CEAS Aeronautical Journal
https://doi.org/10.1007/s13272-025-00934-y

ORIGINAL PAPER

A comparison of numerical and experimental data from wake decay in hovering rotors

Filippo Gajo[1] · **Alexander Heintz**[2] · **Manuel Keßler**[1]

Received: 22 July 2025 / Revised: 3 November 2025 / Accepted: 28 November 2025

Abstract
The study of wake decay of hovering rotors is of significant aerodynamic relevance because of its influence on rotor performance, structural interactions, and safety-critical flight conditions. This paper presents an in-depth numerical and experimental analysis into the wake decay characteristics of hovering rotors, focusing on the evolution of main tip vortices (MTVs) and on the development of secondary structures. The emphasis is on the effects of varying the number of blades and the rotational speeds. Particular attention is given to the detection and comparison of secondary structures, whose accurate identification is challenged by differences in spatial resolution and thus on vortex identification thresholds. Consistent trends with experimental data are identified in high-fidelity numerical simulations regarding the formation and distribution of secondary structures, notably their increase with blade passage frequency (BPF) and distance from the rotor plane. The results demonstrate the ability of numerical simulations to capture the main wake's decay mechanisms for certain BPFs, therefore offering a valuable foundation to further studies on the secondary structures' development and decay.

Keywords Wake decay · Hovering for rotor · Main tip vortex · Secondary structures

1 Introduction

The wake created by a rotor is an important aerodynamic element due to its effects on the rotor performance and on the surrounding elements. The study of wake decay has been an important aerodynamic topic since the 1950s, but recently its importance has grown as there have been increases in the number of rotors in rotorcraft, i.e. advanced air mobility concepts, or in the density of wind farms.

Thus, a detailed analysis of wake decay under a rotor is of scientific relevance. Such an analysis aids in enhancing the design of aircraft by quantifying the aerodynamic interaction between the vortical structures of the wake and other components of the system, i.e. the landing gear and the tail boom for rotorcraft or the tower for windmills. Furthermore, in the case of aircraft, the correct description of the wake decay predicts possible safety problems in particular flight conditions, such as low-altitude flights.

The present study considers a complex, unsteady, three-dimensional flow field in which strong interactions of vortical structures are present (see Fig. 1)). The complexity of these interactions and the subsequent breakdown of the wake are still a challenge for high-resolution numerical simulation. As a result, the analysis of wake decay has been the subject of many investigations [5, 7].

The wake can ideally be divided into different vortical elements (see Fig. 2): the main tip vortex (MTV), the shear layers, and the secondary structures. The helicoidal MTVs, which are well defined in the early wake stages, increasingly interact with the blade shear layers and eventually decompose in a highly turbulent flow field. As illustrated by [11], the interaction appears to involve a mechanism of enrollment of the shear layers by the MTVs to ultimately create vertical vortical structures of lower strengths and s-shapes, i.e. the so-called secondary structures. The shear layer, which plays a fundamental role in this process, is

✉ Filippo Gajo
filippo.gajo@iag.uni-stuttgart.de

Alexander Heintz
alexander.heintz@dlr.de

Manuel Keßler
manuel.kessler@iag.uni-stuttgart.de

[1] Institute for Aerodynamics and Gasdynamics, University of Stuttgart, Wankelstraße 3, 70563 Stuttgart, Germany

[2] German Aerospace Center (DLR), Bunsenstraße 10, 37073 Göttingen, Germany

Published online: 11 December 2025

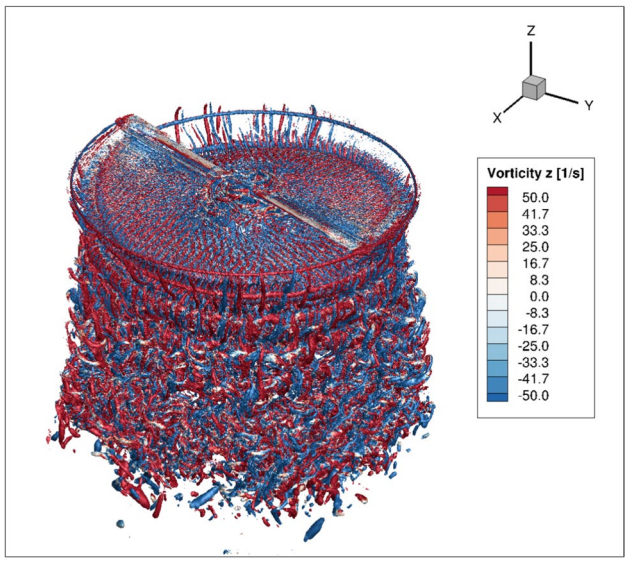

Fig. 1 $\lambda_2 = -0.08$ iso-surface of the 2 blade rotor wake highlighted with the vertical vorticity magnitude

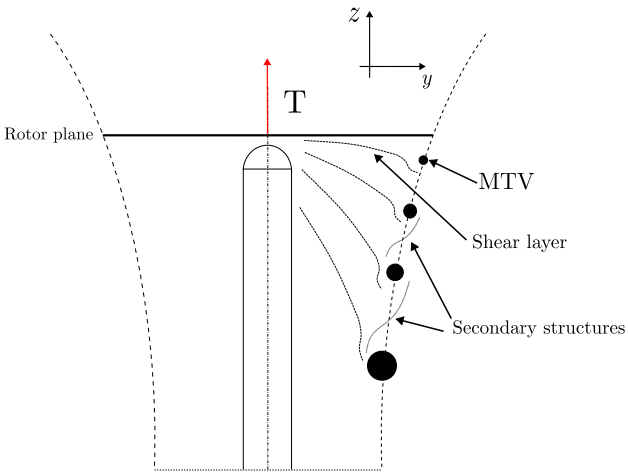

Fig. 2 Schematic description of the main elements on the rotor wake: MTVs, shear layers and secondary structures

formed by small pairs of counterrotating vortices of unequal strengths [19].

The MTV has been analysed in detail through several studies such as [14, 18, 20], and [15]. It evolves from the blade tip and eventually decays in the chaotic pattern described above due to the interactions with the blade shear layers. The transformation of the wake, from the helicoidal vortical structure to the turbulent unsteady state, is not yet fully understood. In fact, the mechanism of vortex decay is a particularly complex topic because it involves not only possible macroscopic instabilities of the MTV helix [12, 21]; and [16], but also the viscous mutual effects as a result of the interactions among vortices.

Secondary structures are key phenomena in wake decay. They were first observed in high-fidelity numerical simulations [1, 7] and the debate of whether they were merely numerical artifacts was considered by [9]. However, their presence was later verified experimentally by [23] with Lagrangian Particle Tracking measurements. These structures are a fundamental feature of vortex decay in a rotating system. Their number increases moving downwards from the rotor plane and is related to the blade passage frequency (BPF) of the rotor itself, as described by [10]. Therefore, the relevance of these structures in the mechanism at the base of the wake decay itself has been demonstrated both experimentally and numerically.

For a deeper understanding of these phenomena, it is necessary to compare and validate highly refined numerical simulations with the sophisticated experimental data, especially far from the rotor plane, where the coherence of the MTV is lost and the amount of secondary structures is very high. This is a very difficult task because of the complexity of the flow field in this region and of the amount of numerical and experimental data that must be processed.

To date, a description of the effects of the numerical parameters on the secondary structure development, such as sub-iterations and the kind of mesh refinement, has been given by [1] and [3]. A complete overview of recent progress in the field is presented in [8]. In particular, [22] presents an experimental and numerical study of secondary structures computed with HELIOS on a two blade rotor with commercially available rotorblades. In this work, the peak of the number of secondary structures is found at z/R = −0.8, below which a reduction can be seen. Moreover, no distinct preferential direction of rotation is detected. A further analysis on the two blade rotor is illustrated by [4]. Here, the focus is on the effects of the numerical and geometrical parameters on the secondary structure characteristics. Specifically, the study examines how changes in rotor thrust and blade pitch angle offset affect wake decay. However, these studies consider only a two blade rotor without fully addressing the problem of comparing experimental and numerical data.

This paper presents a more complete analysis of the numerical and experimental results in terms of MTVs and secondary structures for a hovering rotor with varying number of blades. While the MTV positions can be recovered with a high level of accuracy, the detection of the secondary structures is more demanding. In particular, the difficulty of the task is mainly related to the different resolutions of the grids. This aspect affects both the spatial filters that have to be used and the threshold of the vortex criterion upon which the whole detection method is based. This study offers some modifications to this process in order to find a suitable way to compare the numerical results and the experimental data. These comparisons reveal that numerical simulations can capture a similar increasing trend in the number of

secondary structures propagating downward from the rotor plane. Moreover, the effect of the BPF on the total number of secondary structures is demonstrated as in previous research [10]. Finally, some observations are made on the effect of the number of blades and the blade loading on the circulation of the secondary structures.

2 Experimental setup

The experiments were carried out at the Hover Test Stand (HVG) of the German Aerospace Center (DLR) in Göttingen. The test stand was designed to investigate the aerodynamics of an isolated rotor of $R = 0.76\,\mathrm{m}$ in hover. The rotor height varied between $3.1\,\mathrm{m}$ ($4.1\,R$) and $3.67\,\mathrm{m}$ ($4.8\,R$) above the ground, depending on the height of the traverse. This ensures two main objectives: remaining outside the ground effect and enabling the measurement of secondary vortices at various vortex ages. The rotor hub allows for adjustments in the number of blades, enabling one-, two-, and four-blade configurations. For the measurement of the one blade, an approximately $12\,\mathrm{cm}$ long counterweight was mounted on the opposite side to compensate for the rotor blade imbalance. To measure force and torque, a six-component piezoelectric balance is mounted directly below the propulsion system.

2.1 Particle image velocimetry setup

To investigate primary and secondary vortices, two stereo PIV systems were set up; see Fig. 3. The primary blade tip vortices were measured with a low speed PIV system, operating at approx. $10\,\mathrm{Hz}$. It consists of two pco DIMAX S4 cameras with a resolution of $2024 \times 2024\,\mathrm{px}$, equipped with $85\,\mathrm{mm}$ focal-length lenses and a Quantel TWINS Q-Smart low-speed laser with a pulse energy of about $200\,\mathrm{mJpulse}$. The time delay Δt was set between $\Delta t = 50\,\mu\mathrm{s}$ and $\Delta t = 70\,\mu\mathrm{s}$ depending on the expected hover induced velocity for each case. This results in a field of view (FOV) with a height of about $0.9\,R$ and a width of between $0.46\,R$ at the top and $0.72\,R$ at the bottom. Consequently, an average spatial resolution of $4.85\ \mathrm{px\ mm^{-1}}$ was achieved.

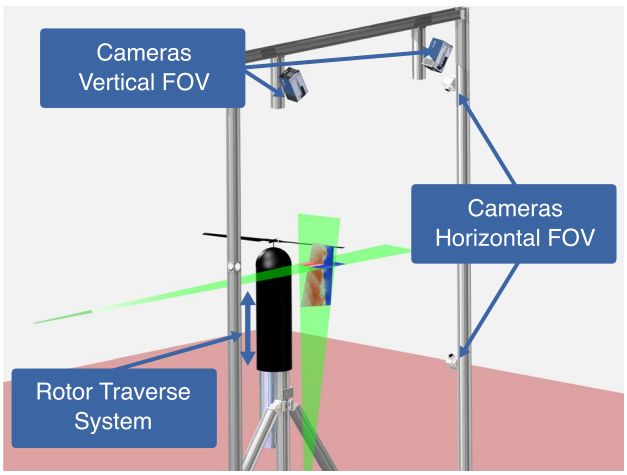

Fig. 3 Measurement setup at the Hover Test Stand (HVG)

To measure secondary vortices (horizontal plane), a high speed PIV setup, operating at $950\,\mathrm{Hz}$ was used. For imaging, two Phantom VEO640L with $130\,\mathrm{mm}$ lenses and a resolution of $2080 \times 2208\,\mathrm{px}$ were used. The illumination was done with a Quantronix DarwinDuo high speed laser, providing an energy output of $26\,\mathrm{mJpulse^{-1}}$. The time delay between the PIV double frames range from $\Delta t = 30\,\mu\mathrm{s}$ to $\Delta t = 50\,\mu\mathrm{s}$, depending on the expected hover induced velocity.

The resulting FOV has a size of about $0.4\,R \times 0.4\,R$ and a pixel size of $0.14\,\mathrm{mm}$ corresponding to $6.93\ \mathrm{pxmm^{-1}}$. The recorded particle images were evaluated with LaVision DaVis 10.2 employing a multi-grid cross-correlation. The final interrogation window size was set to 16 px with $75\,\%$ window overlap, yielding a spatial vector resolution of $0.58\,\mathrm{mm}$ for the horizontal and $0.82\,\mathrm{mm}$ for the vertical plane.

A more detailed description of the experimental setup, measurement timing and PIV processing of this measurement campaign can be found in [10].

3 Numerical setup

The setup described in Sect. 2 has been numerically simulated in the geometry reported in Fig. 4. A simplification has been introduced with respect to the rotor axle that connects the displacement body and the rotor, which is not modeled. For the one blade case, the cylindrical counterweight used in the experimental testcase to balance the whole rotor has been simulated as well. The pitch angle of the numerical test cases have been trimmed to match the total lift generated in the experiments.

The numerical investigation is based on the block structured finite volume RANS CFD code, FLOWer, initially developed by the German Aerospace Center (DLR) and continuously improved for rotorcraft simulations by the research group at the Institute of Aerodynamics and Gasdynamics (IAG) in the University of Stuttgart. The solver is a finite volume code based on a WENO (Weighted Essentially Non-Oscillatory; see [17] of 6^{th} order spatial discretization and 2^{nd} order temporal discretization. The simulations are computed as (DDES-SST) delayed detached eddy simulations with turbulent shear stress transport model ($k-\omega$) with a time step of $\Delta\alpha = 0.25°$, 40 subiterations and $T_{step} \approx 23\,\mathrm{s}$ on 8192 cores. The simulations

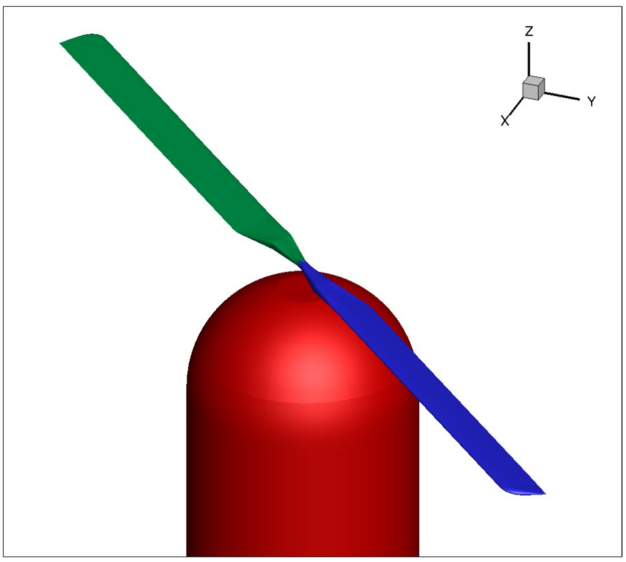

Fig. 4 Geometry of the 2 blade rotor

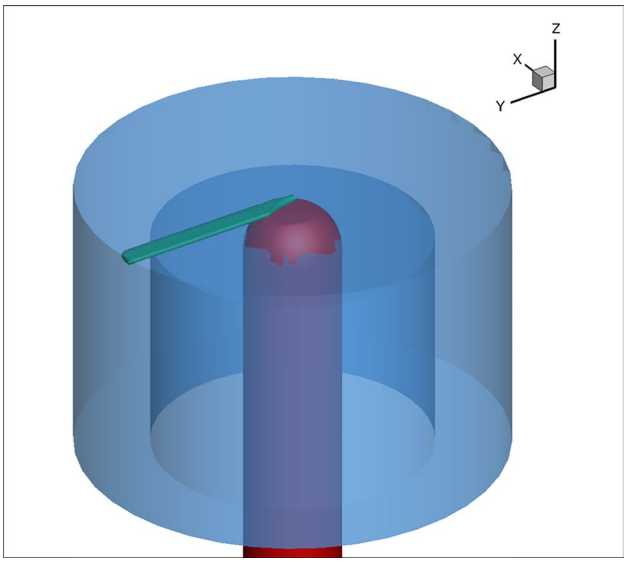

Fig. 5 Different regions of the domain: green is the blade, red is the displacement body and light blue is the 3% C refinement of the background mesh

are computed for 16 revolutions to reach a converged hover condition.

The solver is based on the Chimera technique of [2] to handle the structured mesh. As illustrated in Fig. 5, the mesh is subdivided into different regions, which can be fixed in time or move with the rotor itself, and the results of the calculations are eventually interpolated in the overlapping parts of the computational domain. The first region is highlighted in green, and it is close to the blade: it is devoted to the boundary layer development, and it moves with the rotor. The red zone is the region devoted to the boundary layer on the displacement body, and it does not move in time. Both

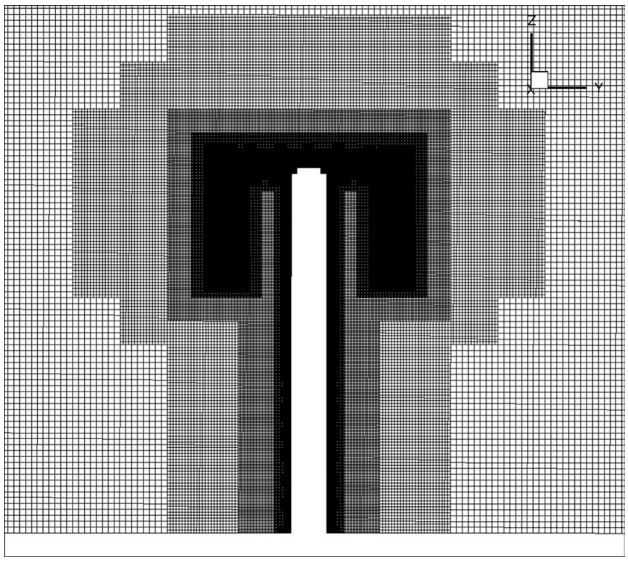

Fig. 6 Mesh refinement.

these regions close to the surfaces are created allowing a value of $y^+ = 1$ on the wall. The blue region encompasses the expected wake position: it does not move and presents a refinement of $3\%C$ with constant size cells.

All these regions are immersed in a background mesh that progressively increases the size of the elements towards the edge of the domain (which is located at $20 \cdot R$) in order to save computational power. The exchange of information among the regions described above and between the refinement and the outer background is achieved through interpolations.

The refinement of the background grid (the blue region) has a toroidal shape, as shown in Fig. 6. This shape is similar to the one analysed by [3] and aims to concentrate the refinement on the region of interaction between the MTVs, the shear layers and the secondary structures. The sizes of the toroid are $0.7 \cdot R$ in the spanwise direction and $1.4 \cdot R$ below the rotor plane. Most of the cells are concentrated in this portion of space, so the computational effort is only slightly affected by the different number of blades of the rotor. Thus, the total number of cells is 288 mil. for the rotor with one blade , 290 mil. for the two blade rotor and 292 mil. for the four blade one.

4 Processing

The MTV detection has been done as following. In the experimental setup, the evaluation is based on the swirling strength (λ_{ci}) criterion and follows the procedure described by [10]. Instead, in the numerical setup the λ_2 criterion (see [13] has been used as the basis for the workflow described by [6]. The methodology applied allows us to detect the

MTV up to late wake ages from the blade position even in the presence of strong disturbances derived by the complex features on the flow field.

In contrast, the post-processing method for detecting secondary structures has focused on applying the established experimental setup described by [10] in the numerical setup, as shown in Fig. 7. The first difference between them is the median filter, which is applied on the velocity components to calculate the Q criterion, to reduce measurement noise. It is not required in the numerical computation of the Q criterion. Furthermore, because the FOV of the PIV measurements does not cover the entire domain of interest, the post processing of the experiments has been adapted accordingly (see [10]. In numerical simulations, the entire domain is considered.

The general idea is to study the secondary structures in horizontal sections defined at different distances from the rotor plane. In each of these planes, the 2D Q criterion is defined as (see [4]:

$$Q = \frac{\partial u}{\partial x}\frac{\partial v}{\partial y} - \frac{\partial u}{\partial y}\frac{\partial v}{\partial x} - \frac{1}{2}\left(\frac{\partial u}{\partial x} + \frac{\partial v}{\partial y}\right)^2 \tag{1}$$

where u and v are the velocities in the plane. The criterion is used to define the position of the vortical structures by means of a set Q-threshold $\overline{Q}$.

The problem has been proved to be particularly relevant due to the different resolutions achieved in the experiments and in the numerics. The different resolutions must be considered in the definition of both the Gaussian filter and the value of the threshold of Q, $\overline{Q}$, above which a region is considered to be inside a vortex.

Regarding the Gaussian filter, which is applied to reduce the noise in both experimental and numerical data, the parameter to be chosen is the standard deviation σ of the filter itself. The following equations have been used:

$$\begin{cases} \sigma_{\text{exp}} = \dfrac{\sigma_{\text{dim}}}{\Delta s_{\text{exp}}} \\ \sigma_{\text{num}} = \dfrac{\sigma_{\text{dim}}}{\Delta s_{\text{num}}} \end{cases} \tag{2}$$

$$\begin{cases} Q = Q_{\text{filtered}} \cdot \sigma_{\text{exp}} \\ Q = Q_{\text{filtered}} \cdot \sigma_{\text{num}} \end{cases} \tag{3}$$

where σ_{dim} is a dimensional quantity defined as $\sigma_{\text{dim}} = 0.003465$ m (see [10], $\Delta s_{\text{exp}} = 0.00054$ m and $\Delta s_{\text{num}} = 0.002$ m are the resolution values of the experimental PIV measurements and numerical setups, respectively, and Q_{filtered} is the Q field filtered by the Gaussian filter.

The magnitude of the velocity gradients is significantly affected by the spatial resolution of the flow field, and vortex identification criteria are highly dependent on these gradients. Consequently, differences in resolution strongly affect the magnitude of Q. To account for this effect, a linear modification of the threshold $\overline{Q}$is applied.

Thus, the following expression has been used:

$$\overline{Q_{\text{num}}} = \overline{Q_{\text{exp}}}\,\frac{\Delta s_{\text{exp}}}{\Delta s_{\text{num}}} \tag{4}$$

where $\overline{Q_{\text{exp}}} = 4.8 \times 10^5$ s^{-2}. The influence of the value of $\overline{Q_{exp}}$ on the detection of secondary structures has been presented by [10]: the value of 4.8×10^5 s^{-2} results as a good compromise between high sensitivity and the exclusion of measurement noise and shear layer vortices in experiments.

The numerical data in Sect. 5 and 6 are computed as follows: after convergence of the numerical simulation, one additional rotation is used to extract data at steps of 5° rotor azimuth. Thus, this leads to 72 distinct flow fields at various azimuthal rotor positions. The data extracted from each of these positions are then averaged on the whole rotation to increase statistical significance. The process is the same for both the MTV and the secondary structures detections.

The experimental data for primary vortices are taken over 50 rotor rotations at 10 different rotor azimuths, resulting in 500 images. In each image, all vortices are detected, and their parameters, e.g., position and circulation, are calculated. Afterwards, the vortices are clustered according to their corresponding vortex age, allowing for the averaging of vortex parameters. For the secondary structures, 2500 images are recorded for each distance from the rotor plane, with each FOV covering about 22.5° rotor azimuth. All detected secondary structures are averaged with respect to

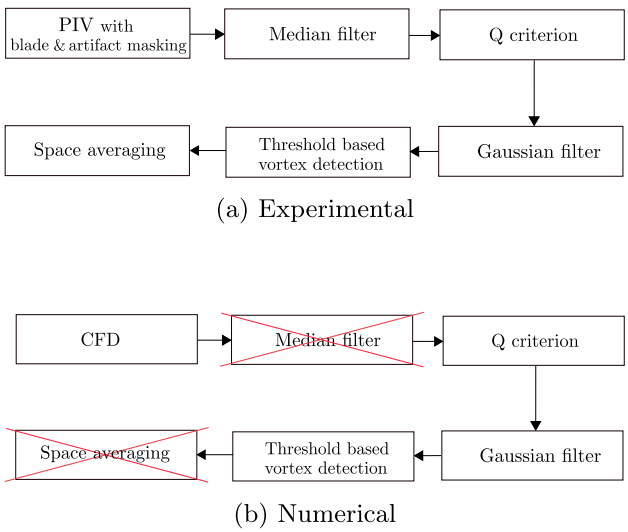

Fig. 7 Comparison of the different post-processing methodologies for the secondary structures detection

one rotor revolution to compute their mean occurrence over 360° azimuth, denoted as N.

5 Main tip vortices

The MTV positions and features have been carefully analyzed because of their relevance to the decay of the rotor wake. The detection process, briefly explained in Sect. 4, has allowed us to compare the numerical and experimental results for the considered rotors, as described in Sect. 2.

5.1 1 blade rotor

The vortex structures present in the flow field of the 1 blade rotor are shown in Fig. 8, where the isosurface of λ_2 is illustrated. The wake structure presents a well defined MTV and eventually some other vertical vortical structures which can be considered as incipient secondary structures. This setup has been of particular relevance to prove the validity of the numerical detection method due to the simplicity of the wake structure.

Figure 9 illustrates the comparison between the experimental data (markers) and the position evaluated from the numerical simulations (lines) at different wake ages (Ψ) from the position of the blade. The blue line and markers are related to the axial position (left y axis), while the red line and markers represent the radial position (right y axis). The MTV positions are computed compared to the tip of the blade, which is placed at $z/R = 0$.

The axial position of the MTV (blue) shows good agreement between the experiments and the numerics up to $\Psi \approx 1450°$. The change in downward velocity due to the first blade passage at $\Psi = 360°$ is also clearly visible. The different overall slope of the axial position after $\Psi = 360°$ is due to the lower pitch angle in the numerical setup, as calculated in the rotor trim study.

Regarding the radial position of the MTV (red), the experiments show a spread of the solution after $\Psi = 500°$ and the numerical position follows the lower values of r/R among the calculated ones.

A relevant aspect is the wandering of the MTV, namely the movement in time of the MTV in axial and radial directions. It is calculated as the standard deviation (Σ) of the positions in a complete rotation of the rotor and follows a trend of monotonic increase (see [14]. In Fig. 10 the experimental data and the numerical results are compared. In experimental data, the radial wandering (red markers) is higher than the axial wandering for $\Psi \geq \approx 360°$. In contrast, in numerical results the axial wandering is higher and it has a trend that is affected by the blade passage. In particular, at late wake ages, there is a periodic reduction

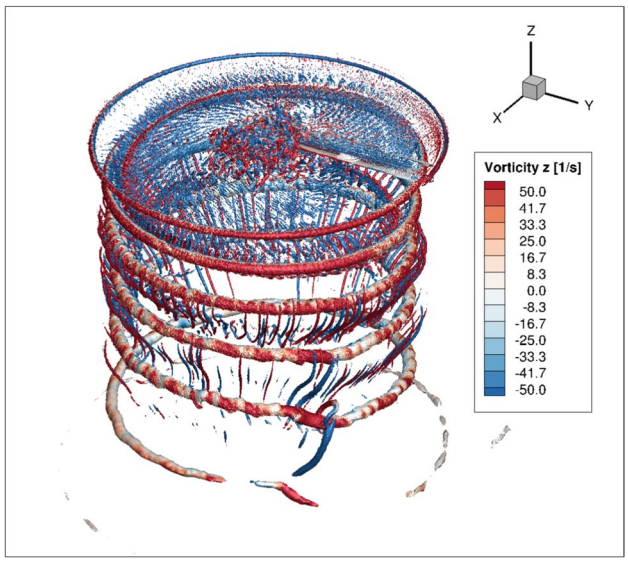

Fig. 8 Isosurface of $\lambda_2 = -0.08$ of the 1 blade rotor and contour of vorticity in the z direction

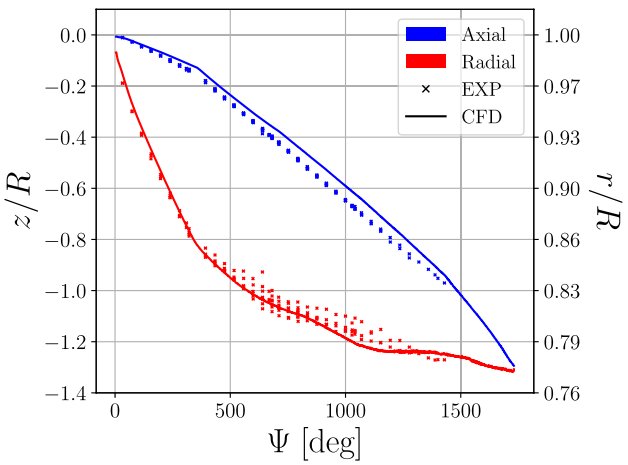

Fig. 9 1 blade rotor: MTV positions comparison between numerical and experimental setups

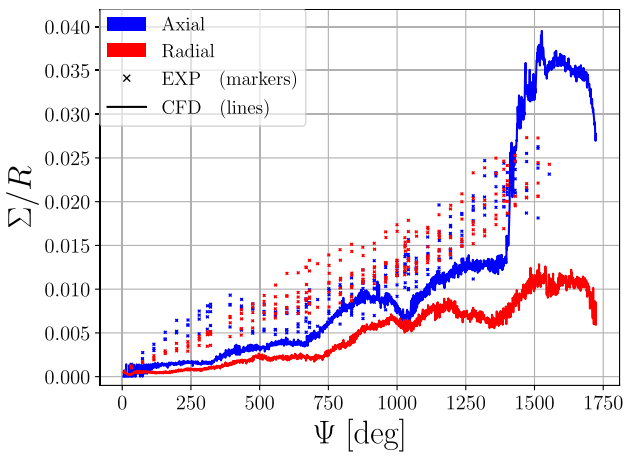

Fig. 10 1 blade rotor: comparison of wandering of the MTV in axial and radial directions

of the wandering in both directions at $\Psi \approx 720°$, $\approx 1080°$ and $\approx 1440°$ (see Fig. 10). In general, the numerical results show a lower wandering of the MTV due to the lower complexity of the wake in Fig. 9, in terms of vortical structures other than the MTV, resulting in fewer stochastic movements of the MTV itself.

5.2 2 blade rotor

Apart from the increase in complexity of the wake structure, the prominent feature found by experiments of the 2 blade rotor is the pairing between the MTVs. Figure 11 shows the position of the MTVs measured in experiments (markers) and calculated with CFD (lines). Each kind of marker and each kind of line represents the MTV that forms from a different blade. The pairing of the MTVs modifies the position of one MTV with respect to the other. As can be seen in Fig. 11, the pairing grows after the first blade passage, so $\Psi \approx 200°$. Most probably, slight imperfections on the experimental blades, e.g. pitch angle and elastic behaviour, trigger the pairing instabilities.

In the numerical solution, for which the rotor geometry of each blade is perfectly identical to the other, the pairing is only slightly present, as also described by [4]. The different slope of the axial position (blue lines and markers) after the first blade passage at $\Psi = 180°$ is again due to the different pitch angle used to match the rotor lift.

Regarding the radial position (red line and markers), the numerical solution is consistent with the position of the blade that is not affected by a movement induced by the pairing (lower set of points).

Figure 12 shows the wandering of the MTV for the 2 blade rotor. The experimental data and the numerical results are consistent up to $\Psi \approx 550°$, above which the numerical results show a strong increase in wandering. This increase is related to two different causes: on the one hand, to mutual inductions of the secondary structures with the MTVs and, on the other hand, to the difficulty of detecting the MTV at very late wake ages due to the strong dissipation of the MTV in numerical simulations compared to the experimental test case.

5.3 4 blade rotor

The wake produced by the 4 blade case is the most complex among the one studied in this work. It is possible to track the position of the MTV up to $\Psi \approx 450°$, as shown in Fig. 13. In this case, no pairing is found and the results agree both axially and radially.

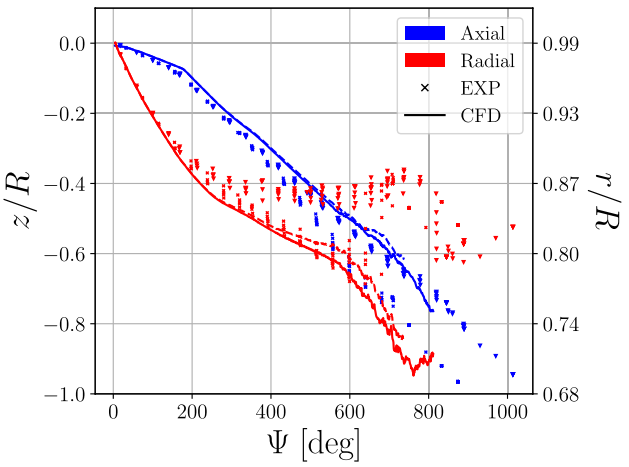

Fig. 11 2 blade rotor: MTV positions comparison between numerical and experimental setups

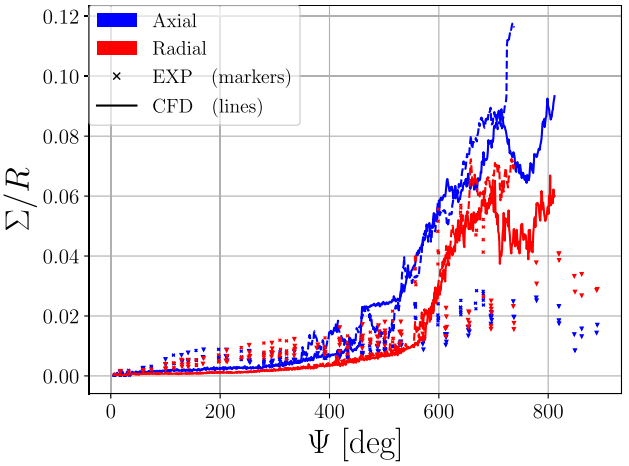

Fig. 12 2 blade rotor: comparison of wandering of the MTV in axial and radial directions

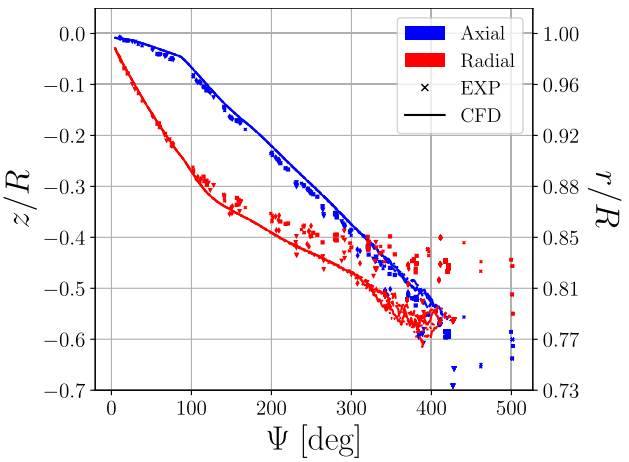

Fig. 13 4 blade rotor: MTV positions comparison between numerical and experimental setups

5.4 Circulation

The circulation of the MTV has been computed[1] and it is illustrated in Fig. 14. The wake age is normalized with respect to the maximum numerical wake age upon which the MTV can be tracked. The radius of integration of the swirl velocity is $R_C = 0.5\ C$ in the experimental setup while in the numerical evaluation $R_C = 0.8\ C$.

The higher integration radius R_C used in numerical simulations is due to the lower resolution achieved with respect to experiments, which causes a more spread vortex. However, increasing the integration radius introduces a drop in circulation just after the first blade passage. This effect, related to the presence of the shear layer, is more evident with higher numbers of blades, and was already described by [6].

The comparison in circulation, as reported in Fig. 14, shows a good agreement of the numerical results with the experiments. This is particularly true for the 1 blade rotor (blue) up to very late wake ages; the 2 blade case presents an overestimate of circulation up to $\Psi \approx 200°$, where the shear layer is considered in the integration radius. The error between the two evaluations is, on average, 7.4 % for $\Psi \leq 200°$. After the region affected by the shear layer (which spans between 20% and 40% of Ψ_{max}), the experimental data are recovered by the numerical solution up to $\Psi = 600°$ (75% of Ψ_{max}); then the circulation computed in the numerical simulation decays faster than in experiments. The four blade rotor is affected by a similar effect of the shear layer on the computed circulation of the two blade rotor. Outside the affected region, the numerical result overestimates the experimental result by around 5.6% on average. Then, after the drop due to the presence of the shear layer, the circulation values are recovered.

The decay of the numerical MTV circulation in the two blade rotor at late wake ages is more relevant with respect to the one and the four blade rotors. Figure 15 shows the evolution of the numerical vortex tangential velocity, adimensionalized with the induced velocity of the rotor, at different wake ages and for the two blade rotor. The vortex tangential velocity is calculated using a time average of the tangential velocity around the vortex centers. Each solid line represents a convolution of the numerical values (markers) used to make the profile smooth.

It is interesting to note the different trends of the tangential velocity profiles at $\Psi = 75\%\ \Psi_{max}$ and at $\Psi = 95\%\ \Psi_{max}$ (brown line). In particular, the profile at $\Psi = 95\%\ \Psi_{max}$ in Fig. 15ashows a rapid decay in the vortex tangential velocity at short distances, similar to vortices at younger wake ages. Thus, even though the detection method still allows to find a MTV in the flow field, the decay of the vortex tangential velocity is almost complete, and it explains the sudden strong decrease of circulation shown in Fig. 14. This is not the case for the one and the four blade rotor, as reported in Fig. 15bfor the $\Psi = 95\%\ \Psi_{max}$.

Figure 16 illustrates the comparison between the experimentally measured radial section (see Fig. 16a) and the numerically calculated ones (see Fig. 16b). These radial sections are computed by an average over an entire rotor rotation and are taken at a fixed distance from the blade position. The out of plane vorticity shows the position of the MTVs and the shear layers. In the numerical data (see Fig. 16b) the MTV is clearly decaying faster than in the experimental results. Furthermore, the shear layer is stronger, especially the counterrotating vortex (blue region) at the end of the shear layer itself. This difference affects the calculation of the circulation shown in Fig. reffig:circulation.

[1] To have the same postprocessing in both numerical simulations and experiments, the formula $\Gamma = \int_C \mathrm{v} \cdot \mathrm{dl}$ is used.

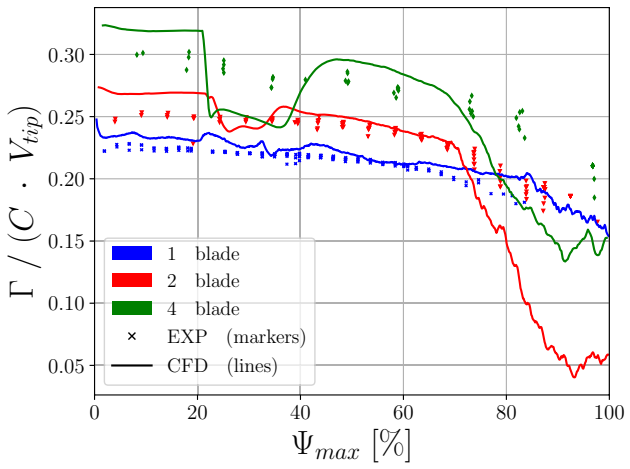

Fig. 14 MTV circulation comparison between numerical and experimental setups for the different rotors considered and at different percentage from the maximum wake age Ψ_{max}

6 Secondary vortices

Secondary structure detection, as described in Sect. 4, is the other key aspect of wake decay analysed in this work. The complexity of the wake structure varies among the cases studied, as can be seen by qualitatively comparing Figs. 8 and 17).

[10] suggest that the number of secondary structures is related to the BPF of the rotor. Thus, different rotors with different rotational speeds, but the same pitch angle of the blade (and therefore the same C_T), have been considered (see Table 1).

Hence, in addition to the 3 base cases (***1 base***, ***2 base*** and ***4 base***), simulations with double rotational speed (***1 aug*** and ***2 aug***) and with reduced rotational speed (***2 red*** has

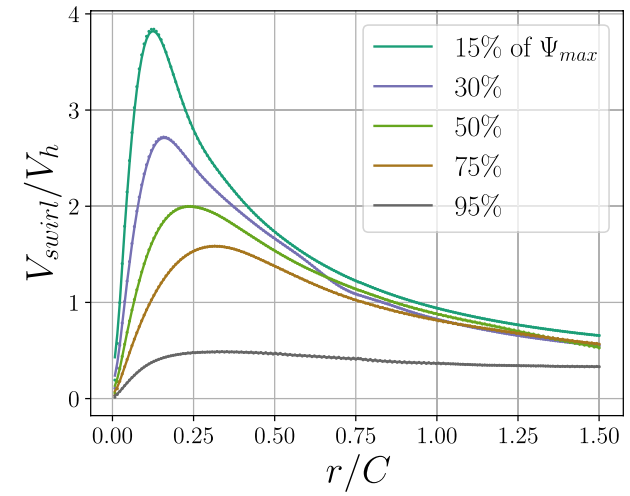

(a) 2 blade rotor

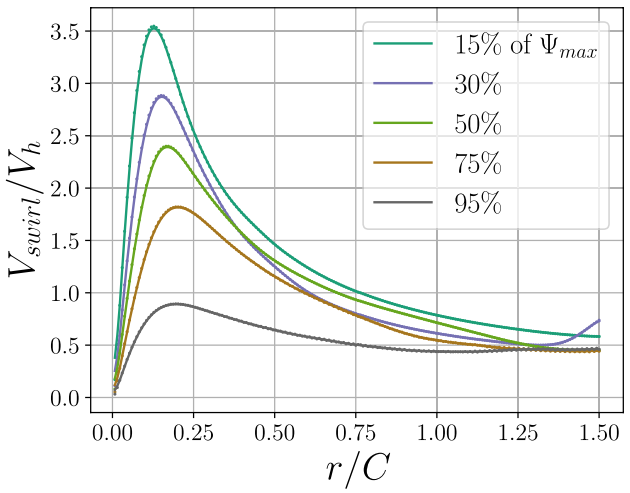

(b) 4 blade rotor

Fig. 15 Average vortex tangential velocity of the MVT at different wake ages for rotors with different blade counts

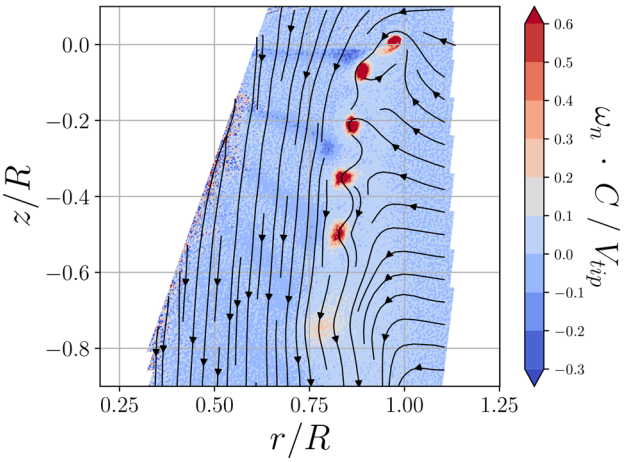

(a) Experiments.

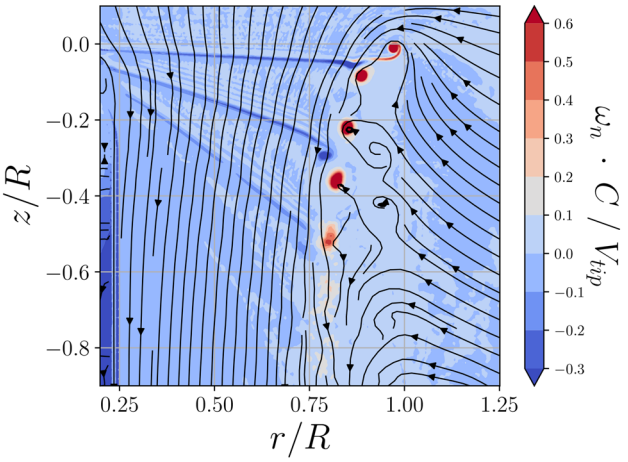

(b) Numerical simulations.

Fig. 16 Radial sections of the out of plane vorticity and streamlines at $\Psi = 200°$: comparison of the 4 blade rotor

$\omega = \omega_{base}/\sqrt{2}$, while ***2 redred*** has $\omega = \omega_{base}/2$) have been computed. Thus, the ***1 aug*** and the ***2 aug*** cases present a different rotational speed but same blade loading with respect to the base cases.

Secondary structures have been studied at different distances downward from the rotor plane in terms of number, circulation strengths, and radial distribution.

The effect of BPF on the number of secondary structures at different axial distances from the rotor plane is shown in Fig. 18. The cases with BPF = 75.5 Hz and 37.8 Hz (blue and red, respectively) show good agreement between the experimental data and the numerical results. In contrast, the cases with BPF = 26.7 Hz and 18.9 Hz do not find any secondary structure in the numerical simulations. This is due to the higher spatial resolutions achieved in the experimental setups with respect to the numerical ones. The resolution affects the dissipation of the grid and ultimately the strengths of the vortices that can be found. Thus, because the numerical resolution is too low to detect the vortices in the cases ***1 base***, ***2 redred*** and ***2 red***, these are of little use in this analysis.

6.1 BPF = 37.8 Hz

The cases ***2 base*** and ***1 aug*** have both BPF = 37.8 Hz. The comparison of the number of secondary structures is shown in Fig. 19. The numerical results of the ***2 base*** case (orange line) do not match the experimental results (blue line) even though the overall increasing trend moving downward from the rotor plane is recovered. In particular, more secondary structures for $-z/R > 0.4$ are detected because

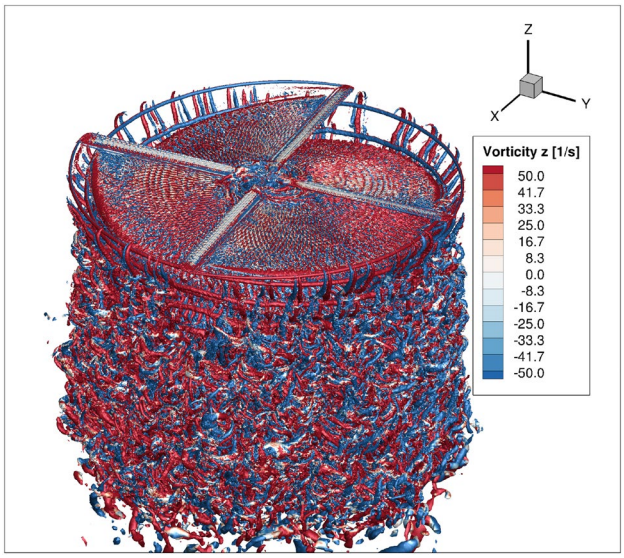

Fig. 17 Isosurface of $\lambda_2 = -0.08$ of the 4 blade rotor highlighted with vorticity in the z direction

Table 1 Numerical cases considered for the secondary structure analysis

Name	N_b	BPF [Hz]	T [N]	Exp
1 base	1	18.9	35.97	yes
2 redred	2	18.9	18.28	yes
2 red	2	26.7	37.85	yes
2 base	2	37.8	74.17	yes
1 aug	1	37.8	152.05	no
4 base	4	75.5	151.53	yes
2 aug	2	75.5	314.01	no

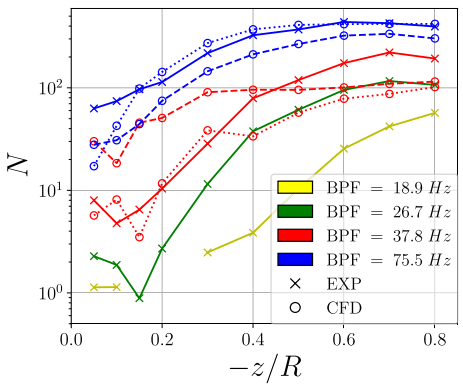

Fig. 18 Number of secondary structures for different BPFs and at different axial distance from the rotor plane

of the presence of a more defined shear layer in numerical simulations. From $-z/R \leq 0.4$ the numerical result is lower than the experimental one due to the higher dissipation in the numerical simulations. Regarding the ***1 aug*** case (green line), for which only numerical results are available (see Table 1), it presents a number of secondary structures.

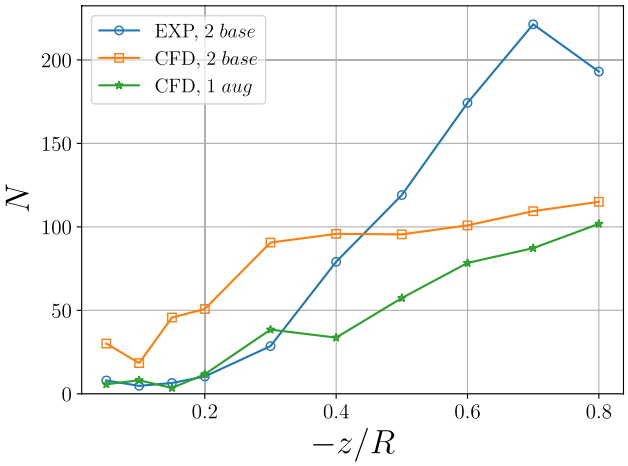

Fig. 19 Comparison of the total number of secondary structures, BPF = 37.8 Hz

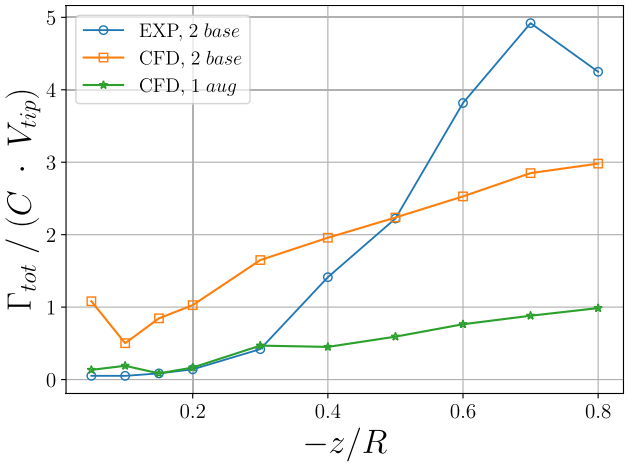

Fig. 20 Comparison of the cumulative circulation of secondary structures, BPF = 37.8 Hz

These structures are less than in the ***2 base*** but more than in the ***1 base***, where none are found.

More relevant is the circulation of the secondary structures, which quantifies their effect on the wake itself. Figure 20 shows the comparison of the cumulative circulation of the secondary structures. For the ***2 base*** case, the trend of the number of secondary structures presented in Fig. 19 is recovered. Regarding the ***1 aug***, the total circulation lags behind the number of secondary structures created. Thus, on average, lower intensity vortices are formed in the ***1 aug*** case than in the ***2 base*** case.

6.2 BPF = 75.5 Hz

The cases ***4 base*** and ***2 aug*** have a BPF = 75.5 Hz. The increase in BPF creates a more chaotic wake with more secondary structures. However, the comparisons between the numerical and the experimental results match better than for

lower values of BPF. The total number of secondary structures is reported in Fig. 21: the trend of the curve and the numerical value of the ***4 base*** (orange line) agree with the experimental result (blue line). However, the number of secondary structures is underestimated in the numerical setup. By contrast, the ***2 aug*** (green line, only numerical cases are available) shows a curve similar to the one of the ***4 base*** case with slightly higher values.

Figure 22 shows the cumulative circulation of the secondary structures. The results for the ***4 base*** cases match very precisely up to $-z/R \leq 0.4$, above which the numerical solution underestimates the total circulation which is due to the dissipation of the numerical results. Thus, numerical simulations are able to find the correct amount of circulation within the secondary structures even though the number of them is not well retrieved because of the impossibility of detecting the weaker structures. The ***2 aug*** presents a total circulation that is lower than the ***4 base*** although the total number of secondary structures detected is slightly higher(see Fig. 21). Thus, the ***2 aug*** case produces more but weaker secondary structures on average than the ***4 base***. Moreover, the cumulative circulation of these structures has no peak for $-z/R = 0.6$.

Figure 23 illustrates the probability density function (PDF) of the distribution of the secondary structure circulations at different distances from the rotor plane. For all positions, but very close to the rotor plane ($-z/R = 0.1$), there is a balance between the number of positive and negative circulation vortices, as already shown by [3]. Moreover, moving downward from the rotor plane, the number of secondary structures increases, but the trend of the distribution is constant, as well as the position of the peaks. Comparison of the ***4 base*** cases (blue and orange lines) shows that the numerical results are unable to find the right amount of weaker structures while the amount of stronger structures is recovered and even overestimated in the lower stations ($-z/R = 0.5$ or 0.6). This is in agreement with the fact that numerical simulations have a larger dissipation. The ***2 aug*** (green line) still exhibits symmetric curve trends, but the peaks are at lower values of circulation with respect to the ***4 base*** case and more weaker structures are recovered. That aspect explains the low total circulation shown in Fig. 22 despite the large number of secondary structures detected. Thus, even increasing the blade loading and subsequently the strengths of the MTVs, the secondary structures are weaker than in the ***4 base*** case. This leads to the conclusion that the strength of the secondary structures is not primarily related to the MTV strength but to the number of shear layers, and thus ultimately to the number of blades of the rotor.

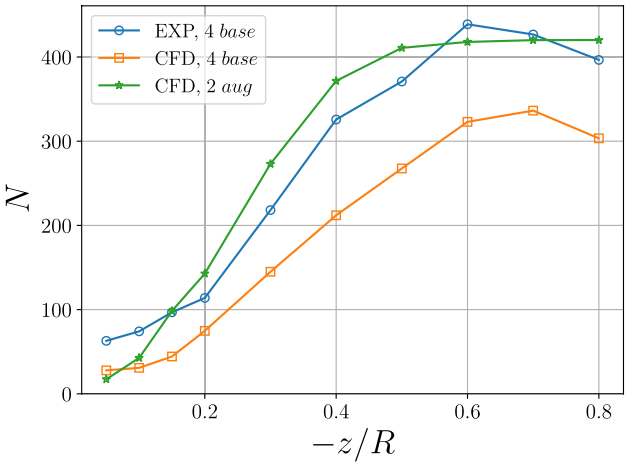

Fig. 21 Comparison of the total number of secondary structures, BPF = 75.5 Hz

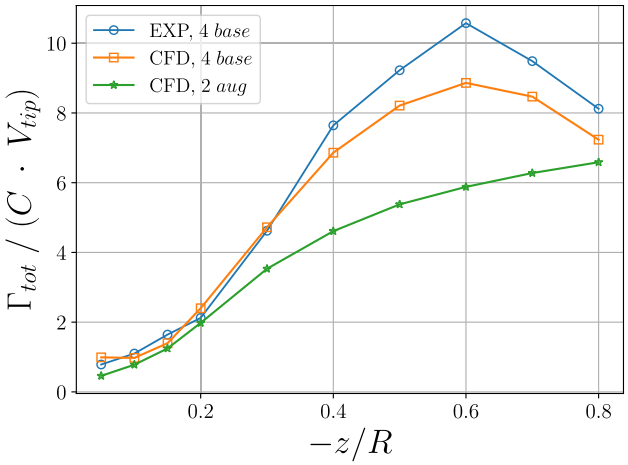

Fig. 22 Comparison of the cumulative circulation of secondary structures, BPF = 75.5 Hz

7 Conclusion

This paper addresses the problem of studying the wake decay of a rotor in hover with different numbers of blades, which ultimately affects the complexity of the vortical structures inside the wake and leads to different blade loading. The experimental data, measured through differently oriented PIV planes, are compared to high fidelity numerical simulations computed with the structured flow-solver code FLOWer.

Regarding the MTV comparison, a good agreement is found between numerical results and experimental data in terms of position, vortex circulation, and wandering, i.e. the temporal movement of the MTV. The one blade rotor has a well-defined MTV up to very late wake ages and it is possible to track it up to $-z/R = 1.2$ and $\Psi = 1750°$. Furthermore, in the numerical simulation the wandering of

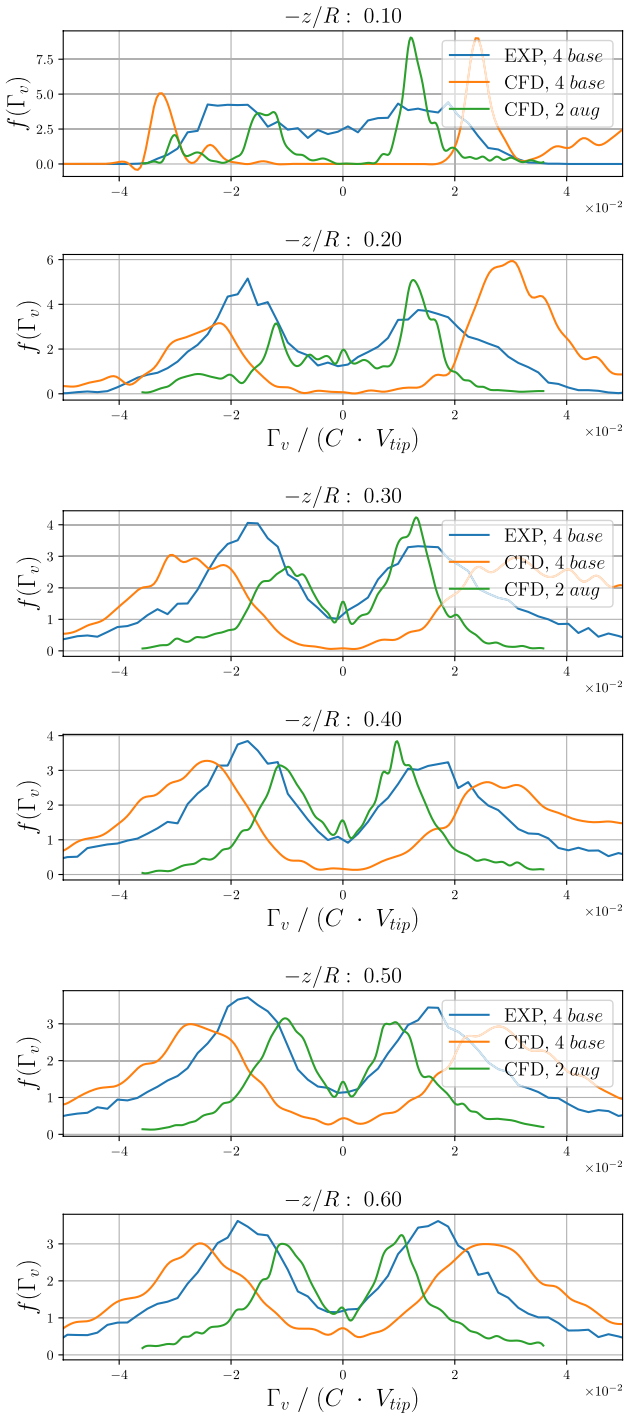

Fig. 23 PDF of the distribution of the circulation of the secondary structures at different distances from the rotor plane, BPF = 75.5 Hz

the MTV is lower compared to the experimental data and stronger in the axial direction than in the radial one.

The two blade rotor is characterised by a pairing of the MTV, which is only slightly recovered in the numerical setup (similarly to [4]. However, the position and circulation of the MTV are well recovered in the numerical results. Regarding the MTV wandering, it increases because of the larger number of secondary structures and resulting vortical mutual inductions. However, axial wandering remains predominant with respect to radial wandering, in contrast to the experimental data. The four blade case, which is the most complex flow field, shows that no pairing is present on the MTV and that a good agreement between the numerical and the experimental results is achieved.

The MTV circulation can be calculated; the results are highly accurate for the one blade rotor up to very late wake ages. However, for the two and four blade rotors, the accuracy decreases in the range between 20% and 40% of Ψ_{max} due to the stronger shear layer observed in the numerical simulations.

Detecting secondary structures has proven challenging because of the differing resolutions of the numerical and experimental setups. Through the modification of both the Gaussian filter applied in the post-processing and the threshold of the Q-criterion, it is possible to compensate for the problem. Different simulations have been performed to provide a more comprehensive analysis of the effect of the BPF on the development of the secondary structures. In addition, the influence of the number of blades on the circulation distribution of secondary structures has been examined. The formation of secondary structures follows from a reorganisation of the vorticity of the MTV and the shear layers into coherent structures through the mechanism of vortex stretching, contrasting viscous diffusion which ultimately leads to the creation of secondary structures. These vortices are subjected to a temporal decay in strength.

The effect of the BPF, at constant blade loading, is to increase the total number of secondary structures, as illustrated by [10]. This effect is also retrieved in the numerical simulations: in particular, the increase of BPF increases the total number of structures. The lower resolution of the numerical simulation precludes the possibility of detecting any secondary structure for low values of BPF (18.9 and 26.7 Hz). For a BPF = 37.8 Hz, the number of secondary structures and their total circulation, calculated from the numerical data, follow the general trend observed in the experimental results. However, these data are affected by the shear layer close to the rotor plane and by the higher dissipation far from it. Thus, the numerical and experimental values are not accurate with respect to each other. In contrast, the comparison with BPF = 75.5 Hz shows a high level of consistency in the results, especially in terms of the total circulation. The analysis of the circulation distribution illustrates that the numerical simulations correctly capture the number of stronger structures, while the weaker ones are underestimated due to the dissipation of the grid.

Furthermore, simulations with a fixed blade pitch but different rotation speeds have been conducted. The results,

as well as the circulation of the secondary structures, show that these structures are indeed affected by the number of blades. In particular, reducing the number of blades induces a change in the distribution of circulation of the secondary structures with the detection of a larger number of weaker vortices. Thus, the shear layer position appears to be the primary factor in the formation of the secondary structures, whereas the MTV strength plays a less significant role.

In conclusion, high fidelity numerical simulations are a feasible way to achieve a comprehensive insight into the main features of the wake decay in a hovering rotor. However, these simulations are subject to certain limitations in terms of the detection of secondary structures. Given the increasing computational power available, further studies on the development and on the decay of the secondary structures can be conducted with a particular focus on the overall effects of the blade loading.

Acknowledgements This investigation was partly funded by Deutsche Forschungsgemeinschaft (DFG) under grant number KR 2959/8-1 (Filippo Gajo) and RA 1046/4-1 (Alexander Heintz). The authors gratefully acknowledge the German Aerospace Center (DLR) for access to the FLOWer code, and the High Performance Computing Center Stuttgart (HLRS) for computational resources and support on the Hawk cluster.

Author contributions F.G. wrote most of the manoscript and did the numerical part; A.H. did the experimental setup and the Section 2 of the test. All the authors reviewed the manoscript.

Funding Open Access funding enabled and organized by Projekt DEAL.

Data availability No datasets were generated or analysed during the current study.

Declarations

Conflict of interest The authors declare no conflict of interest.

References

1. Abras, J., Hariharan, N., Narducci, R.: Wake breakdown of high-fidelity simulations of a rotor in hover. Am. Inst. Aeronaut. Astronaut. (2019). https://doi.org/10.2514/6.2019-0593
2. Benek, J.A, Buning, P.G., Steger, J.L., et al.: Chimera: a grid-embedding technique. Tech. Rep. NASA TM-110052, NASA Ames Research Center (1986)
3. Bodling, A., Potsdam, M.: Numerical investigation of secondary vortex structures in a rotor wake. J. Am. Helicopter Soc. **67**(4), 1–18 (2022). https://doi.org/10.4050/JAHS.67.042007
4. Bodling, A., Schwarz, C., Wolf, C.C., et al.: Enhancing numerical accuracy in the prediction of rotor wake vortex structures. Phys. Fluids **36**(3), 037137 (2024). https://doi.org/10.1063/5.0196010
5. Chaderjian, N., Buning, P.: High resolution Navier-Stokes simulation of rotor wakes. Annu Forum Proc AHS Int **1**, 375–392 (2011)
6. Gajo, F., Keßler, M.: Challenges about detecting and analysing the rotor blade tip vortices in numerical simulations at late wake ages. In: 50th European Rotorcraft Forum, Marseille (2024)
7. Hariharan, N., Egolf, T., Sankar, L.: Simulation of Rotor in Hover: Current State, Challenges and Standardized Evaluation. American Institute of Aeronautics and Astronautics, National Harbor. https://doi.org/10.2514/6.2014-0041
8. Hariharan, N., Abras, J., Narducci, R.: An overview of wake breakdown in high-fidelity simulations of rotor-in-hover. pp 1–22. https://doi.org/10.4050/F-0076-2020-16473 (2020)
9. Hariharan, N.S., Egolf, T.A., Narducci, R., et al.: Helicopter rotor aerodynamic modeling in hover: Aiaa standardized hover evaluations. In: 53rd AIAA Aerospace Sciences Meeting. https://doi.org/10.2514/6.2015-1242 (2015)
10. Heintz, A., Schwarz, C., Wolf, C.C., et al.: Configurational influence on a vortex system of a hovering rotor. AIAA J. 1–16. https://doi.org/10.2514/1.J064640 (2025)
11. Heintz, A.J., Schwarz, C., Wolf, C.C., et al.: Influence of configurational parameters on the vortex system of a rotor in hover. In: AIAA SCITECH 2024 Forum. American Institute of Aeronautics and Astronautics, AIAA SciTech Forum (2024). https://doi.org/10.2514/6.2024-0896
12. Jain, R., Conlisk, A.: Interaction of tip-vortices in the wake of a two-bladed rotor in axial flight. J. Am. Helicopter Soc. (2000). https://doi.org/10.4050/JAHS.45.157
13. Jeong, J., Hussain, F.: On the identification of a vortex. J. Fluid Mech. **285**, 69–94 (1995). https://doi.org/10.1017/S0022112095000462
14. Kindler, K., Mulleners, K., Richard, H., et al.: Aperiodicity in the near field of full-scale rotor blade tip vortices. Exp. Fluids **50**, 1601–1610 (2011). https://doi.org/10.1007/s00348-010-1016-8
15. Leishman, J.G.: Measurements of the aperiodic wake of a hovering rotor. Exp. Fluids **25**, 352–361 (1998). https://doi.org/10.1007/s003480050240
16. Leweke, T., Quaranta, H., Bolnot, H., et al.: Long- and short-wave instabilities in helical vortices. J. Phys. Conf. Ser. **524**, 012154 (2014). https://doi.org/10.1088/1742-6596/524/1/012154
17. Liu, X.D., Osher, S., Chan, T.: Weighted essentially non-oscillatory schemes. J. Comput. Phys. **115**(1), 200–212 (1994). https://doi.org/10.1006/jcph.1994.1187
18. Martin, P.B., Leishman, J.G.: Trailing vortex measurements in the wake of a hovering rotor blade with various tip shapes. In: 58th Annual Forum of the American Helicopter Society, Montréal, Canada, preprint in NASA Technical Reports Server (TRS Doc ID 20030071150, publication date January 1 2003) (2002)
19. Milluzzo, J., Leishman, J.G.: Fluid dynamics of the helicoidal wake sheets trailed from a hovering rotor. J. Am. Helicopter Soc. **1**(61), 1–17 (2016). https://doi.org/10.4050/JAHS.61.012002

20. Mula, S., Stephenson, J., Tinney, C., et al.: Dynamical characteristics of the tip vortex from a four-bladed rotor in hover. Exp. Fluids (2013). https://doi.org/10.1007/s00348-013-1600-9
21. Okulov, V., Sørensen, J.: Instability of a vortex wake behind wind turbines. Dokl. Phys. **49**, 772–777 (2004). https://doi.org/10.1134/1.1848637
22. Schwarz, C., Bodling, A., Wolf, C.C., et al.: Development of secondary vortex structures in rotor wakes. Exp. Fluids **63**, 4 (2022). https://doi.org/10.1007/s00348-021-03348-8
23. Wolf, C.C., Schwarz, C., Kaufmann, K., et al.: Experimental study of secondary structures in a rotor wake. Exp. Fluids **60**(11), 175 (2019). https://doi.org/10.1007/s00348-019-2807-1